



BiOCl micro-assemblies consisting of ultrafine nanoplates: A high performance electro-catalyst for air electrode of Al–air batteries

Jinlan Yuan^{a,b}, Jin Wang^c, Yiyi She^d, Jing Hu^a, Pengpeng Tao^a, Fucong Lv^b,
Zhouguang Lu^{b,*}, Yingying Gu^{a,*}

^a Key Laboratory of Resource Chemistry of Nonferrous Metals, Ministry of Education, College of Chemistry and Chemical Engineering, Central South University, Changsha 410083, China

^b Department of Materials Science and Engineering, South University of Science and Technology of China, Shenzhen, Guangdong 518055, China

^c Graduate School at Shenzhen, Tsinghua University, 518055 Shenzhen, China

^d Department of Physics and Materials Science, City University of Hong Kong, Hong Kong, China

HIGHLIGHTS

- BiOCl micro-assemblies consisting of ultrafine nanoplates.
- Excellent oxygen reduction properties.
- Novel catalyst for air electrode of aluminum air batteries.
- The electro-catalytic activity is closely related to the density of oxygen vacancy on the surface of the BiOCl samples.
- A higher ratio of the {001} facets in BiOCl crystals is favorable for the enhancement of the electrocatalytic activity.

ARTICLE INFO

Article history:

Received 25 November 2013

Received in revised form

3 April 2014

Accepted 4 April 2014

Available online 13 April 2014

Keywords:

Bismuth oxychloride

Micro-assemblies

Catalytic properties

Oxygen reduction reaction

Air electrode

Metal–air batteries

ABSTRACT

BiOCl micro-assemblies appearing spherical and plate-like in shape consisting of ultrafine nanoplates were successfully synthesized by a simple hydrothermal method. The obtained BiOCl micro-assemblies were characterized as oxygen reduction reaction (ORR) catalyst for air electrode of aluminum air batteries by using linear polarization and constant-current discharge techniques. The effect of precursor concentration on the electrochemical properties of the air electrodes based on the synthesized BiOCl micro-assemblies was intensively investigated. The results demonstrated that the BiOCl catalyst exhibited promising ORR performance. Koutecky–Levich analysis indicated that a two-electron reaction was favored for the ORR mechanism of the BiOCl (0.18) sample.

© 2014 Elsevier B.V. All rights reserved.

1. Introduction

It has become very urgent to develop safe, green and sustainable energy resources. One of the most attractive clean energy resources is metal–air batteries due to its several advantages including abundance in resources, low emissions [1,2], portability, high energy density, being light weight [3–5], and very low noise and vibrations [6,7]. Additionally, aluminum possesses high energy

capacity (2980 Ah kg^{−1}) and has a very negative value of standard electrode potential of −1.66 V vs. normal hydrogen electrode. Furthermore it is low cost and environmentally friendly. Thus Al–air battery is a promising power source and energy storage device [8–10]. However currently, it is still a challenge to widely commercialize the Al–air batteries [11]. One of the critical obstacles is the relative low power capability of aluminum/air batteries. The key approach to realize this purpose is to create a stable and highly efficient air electrode with low over-potential under high discharge current density [12]. Great efforts have been tried to explore catalysts having high activity and being economically competitive. The generally used precious Pt was replaced by some other inexpensive catalyst such as MnO₂ [13–15], perovskite oxides

* Corresponding authors.

E-mail addresses: luzg@sustc.edu.cn (Z. Lu), guyy02@163.com (Y. Gu).

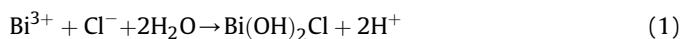
[16], etc. Especially, the manganese dioxide (MnO_2) is considered as one of the most efficient catalyst for the ORR in alkaline medium to replace the costive Pt catalysts [17], due to its environmental compatibility, low cost, and the high electrocatalytic activity. The oxygen reduction reaction (ORR) is the central procedure of the cathodic reaction in fuel cell or metal–air battery. The activity and mechanism by which the ORR takes place in these materials remains to be fully understood, even though the mechanism of the ORR catalyzed by manganese oxide has been extensively studied [18]. The studies have demonstrated that the ORR proceeds on MnO_2 by two main routes: one is the complete four-electron reduction pathway; another is the hydrogen peroxide pathway [19–23]. However, most of the catalysts reported in the literature adopted a two-electron reduction of O_2 to produce H_2O_2 [24–26]. Only a few catalysts have been reported to achieve the four-electron reduction of O_2 [27], such as, macrocyclic compounds and biomimetic materials [28,29].

Bismuth oxychloride (BiOCl) is generally considered as excellent photocatalysts for water splitting and degradation of organic contaminants [30–33]. Other important applications can be found in pharmaceuticals [34]. However, to the best of our knowledge, there are no reports on the application of BiOCl as catalyst for air electrode of metal air batteries. In this article, we intensively investigate the ORR performance of catalyst based on BiOCl micro-assemblies consisting of ultrafine nanoplates for making air cathode. The BiOCl with phase-pure tetragonal crystal structure adopting a micro-assemble morphology consisting of ultrafine nanoplates was synthesized by hydrothermal method. Its catalytic performance towards the ORR was evaluated in a home-made aluminum/air battery model under alkaline conditions. The mechanisms of oxygen vacancy formation and functions in air electrode catalytic reaction were also discussed in detail.

2. Experimental section

2.1. Preparation of materials

The BiOCl particles were fabricated by a hydrothermal method. In the procedure, stoichiometric amount of NH_4Cl was dissolved in 40 mL of distilled water. BiCl_3 was then added slowly under vigorously stirring. Sodium hydroxide was then used to adjust the pH of the solution to be 3. The resultant suspension was stirred for 3 h at 25 °C. Then the mixtures were sealed in a 100 mL Teflon-lined stainless steel autoclave and remained at 180 °C for 6 h. After naturally cooling to room temperature, the products were collected by filtration and washed with distilled water and ethanol for several times. Adding NH_4Cl not only provides Cl^- required for reaction but also decreases the pH value of the reaction solution to control the hydrolysis rate. The reactions proceeded in the following equations:



Based on the reactions (1) and (2), if the Bi^{3+} concentration is too high, $\text{Bi}(\text{OH})_2\text{Cl}$ crystals with very broad particle-size distribution will be quickly formed; while if the Bi^{3+} concentration is too low, it might be hard to get BiOCl precipitates. Consequently, an appropriate BiCl_3 concentration is necessary.

The flower-like BiOCl was prepared according to the literature procedure [35]. 1.96 g $\text{Bi}(\text{NO}_3)_3 \cdot 5\text{H}_2\text{O}$ and 1.31 g cetyltrimethyl ammonium chloride (CTAC) were dissolved in 80 mL ethylene glycol (EG). pH of the solution was then adjusted to 1.0 with KOH/EG solution (1.0 M). The resulting solution was then kept at 160 °C for 12 h

in a 100 mL Teflon-lined stainless autoclave. In order to avoid the possible interference of organic species, the obtained powder was irradiated with ultraviolet light for 2 h after careful washing. The commercial available $\gamma\text{-MnO}_2$ was used as the reference catalyst.

2.2. Preparation of air electrode

The active layer of air electrode was prepared by spraying a mixture of 5 wt% polytetrafluoro-ethylene (PTFE) emulsion, catalysts, active carbon, acetylene black, and an appropriate amount of alcohol. Firstly, the catalysts, active carbon and acetylene black, and PTFE with the mass ratio of 3.5:3.5:1:2 were mixed in appropriate alcohol, and then grinded in an agate mortar for 30 min to form homogeneous slurry. Then this slurry was stirred at 90 °C to remove the alcohol solvent. After the homogeneous slurry turned into paste, it was rolled until the thickness of this layer was about 0.2 mm. The air electrode consists of one gas diffusion layer (the thickness of this layer was about 0.2 mm), Ni-foam current collecting layer and one active layer. The thickness of air electrode was in the range of 0.4–0.6 mm. Finally, the air electrodes were sintered at 320 °C for 30 min at muffle furnace in air atmosphere. After this sintering process, the PTFE particles or fibrils could be transformed into a honeycomb network of thin film. So, more micropores in the air electrode would be formed.

2.3. Catalysts characterization

The phase structures of the samples were analyzed by using a D/Max 2500 X-ray diffractometer with a $\text{Cu K}\alpha$ radiation source of $\lambda = 0.15406$ nm, voltage of 40 kV, current of 250 mA, and a scanning rate of $8.0^\circ \text{ min}^{-1}$. N_2 adsorption isotherms were recorded using a V-Sorb 2800P instrument. Before the measurement, the samples were degassed at 150 °C for 3 h under vacuum. The specific surface area was calculated by using the BET equation from the adsorption isotherm. Morphology was examined by scanning electron microscope using a Hitachi X650 with a voltage of 20.00 kV. The TEM/HRTEM characterizations were carried out in a JEOL JEM-2010 (JEOL Ltd., Tokyo, Japan) at 200 kV.

2.4. Electrochemical characterization

A three-electrode cell was assembled for the electrochemical measurements. A galvanostatic method was employed in this experiment to determine the cathodic polarization curve. A CHI660A electrochemical workstation was used with Hg/HgO as the reference electrode, platinum electrode (1 cm × 1 cm square) as auxiliary electrode, and air electrode as working electrode. The area of the air electrode was fixed at 0.4 cm^2 . The diffusion layer was exposed to air, the catalytic layer was in direct contact with the electrolyte and a 6 mol L^{-1} KOH aqueous solution without CO_2 scrubbing was used as electrolyte. The scanning potential was ranging from 0 to -0.6 V (vs. Hg/HgO) with a scanning rate of 0.002 V s^{-1} . The cyclic voltammograms were recorded in 6 M KOH at a scan rate of 50 mV s^{-1} . A LAND battery testing system was used to measure the discharge curve using aluminum plate as the anode and the air electrode based on the catalysts as cathode. The area of the air electrode was 0.4 cm^2 and the current density was varied between 50, 100, and 200 mA cm^{-2} , respectively. Rotating Disk Electrode (RDE) voltammetry was performed on a MSR electrode rotator (Pine Instrument) and recorded on the CHI 700E potentiostat at a scan rate of 10 mV s^{-1} . A catalyst-modified glassy carbon (GC) electrode (5 mm diameter) was used as the working electrode, and a Pt wire and a Hg/HgO electrode were used as the counter and reference electrodes, respectively. 0.1 M KOH solution was used as the electrolyte.

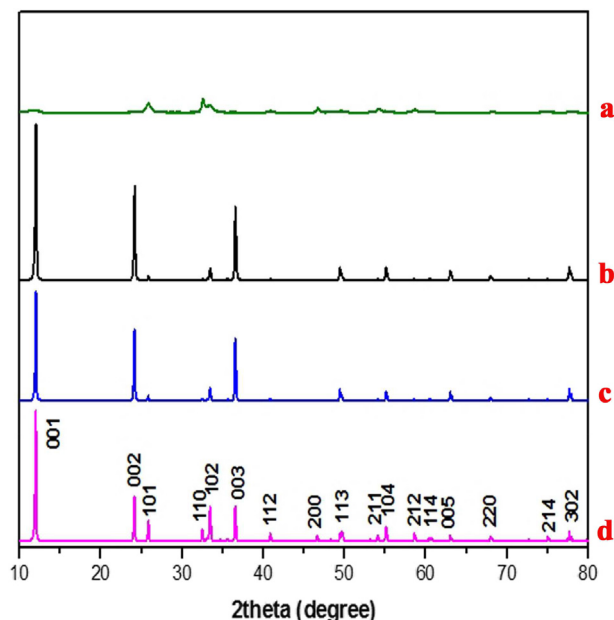


Fig. 1. Powder XRD of the BiOCl with different precursor concentration. (a) Flower-like BiOCl, (b) 0.18 M, (c) 0.06 M, and (d) 0.22 M.

3. Results and discussion

3.1. XRD

The XRD pattern of the prepared BiOCl is shown in Fig. 1. We can see that all the diffractions can be indexed to tetragonal phase of BiOCl with a space group of $P4/nmm$ (129) and lattice constants of $a = b = 3.891 \text{ \AA}$ and $c = 7.369 \text{ \AA}$ according to JCPDS 06-0249. For the BiOCl micro-assemblies, the (001), (002) and (003) diffraction peaks

are sharper and stronger as compared with the (110) peak. It indicates that the BiOCl crystals preferably grew along the c axis ((001) orientations perpendicular to the platelets. No peaks of any other phases or impurities are observed, indicating the high purity of the obtained products. While for the flower-like BiOCl, the three peaks of (001), (002) and (003) diffraction are very weak and the (110) peak is relatively strong. It suggests that the flower-like BiOCl particles favored to grow along the (110) orientations which are perpendicular to the c axis, forming very thin slabs.

3.2. SEM and TEM

Fig. 2 shows the scanning electron microscope of the BiOCl samples. For the BiOCl micro-assemblies, irrespective of the concentration, mainly two kinds of particles showing the morphology of micro-sphere and micro-plates were observed. And both the microspheres and microplates were actually assemblies comprising of ultrafine nanoplates. For the sample with a precursor concentration of 0.06 M, in addition to the micro-plates and microspheres, there are large amount of ultrafine nanoplate-like particles (Fig. 2a). When the precursor concentration was increased to 0.18 M, the amount of ultrafine nanoplates decreased and the micro-plates became more evident (Fig. 2b). The microspheres with a size of about 2 \mu m and microplates with a size ranging from 1 to 10 \mu m dominated the samples. Furthermore, it becomes more obvious that the microplates are actually composed of very thin platelet-like nanoparticles (Fig. 2b). Noticeably, after the concentration was increased to 0.22 M, platelet-like nanoparticles with size of about 100 nm are prevailing the samples in addition to a few microspheres (Fig. 2c). It is clear that the spherical and platelet-like microparticles de-assembled into ultrafine nanoplates at a high precursor concentration. Therefore, precursor concentration has profound effect on the morphology of the BiOCl product. However, the as-prepared flower-like powder was composed of numerous BiOCl nanoplates as shown in Fig. 2d.

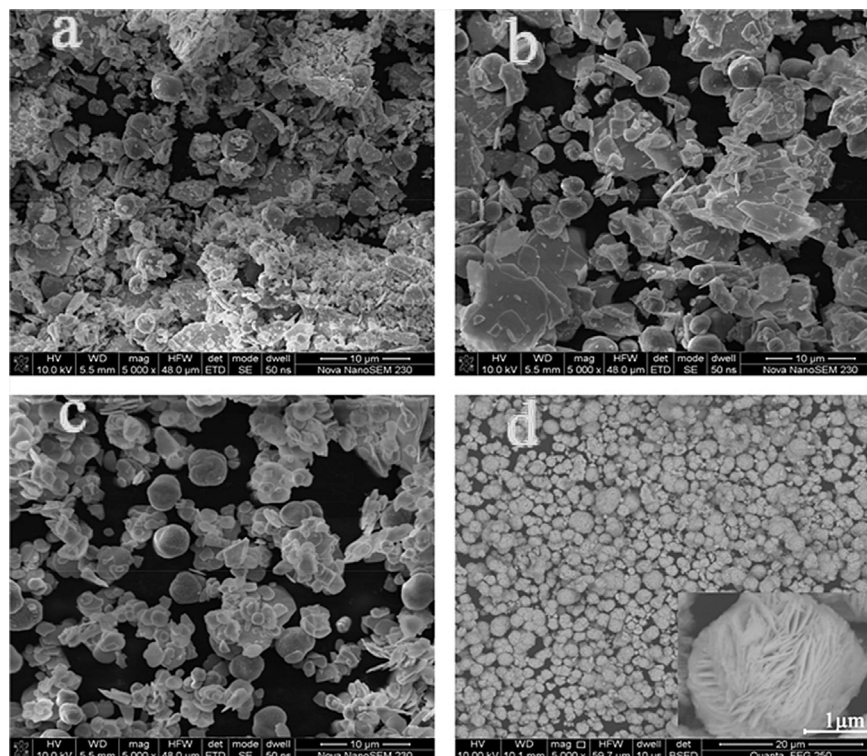


Fig. 2. SEM images of the BiOCl powder prepared under different precursor concentration: (a) 0.06 M, (b) 0.18 M, (c) 0.22 M, and (d) flower-like BiOCl.

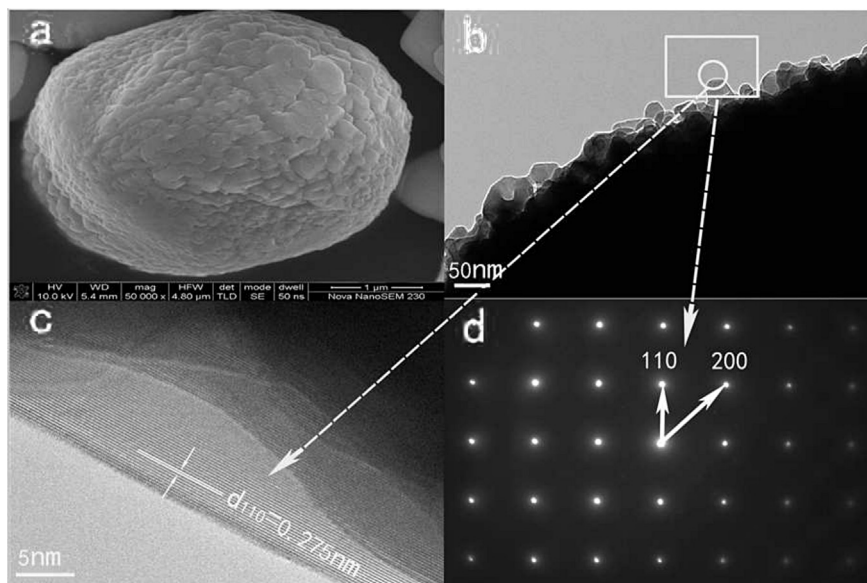


Fig. 3. High resolution (a) SEM and (b, c) TEM images of the spherical particles, (d) shows the corresponding SAED pattern.

Figs. 3a and 4a show the typical SEM image of the BiOCl (0.18) (the sample prepared by using 0.18 M BiCl_3 precursor concentration) microspheres and microplatelets, respectively. Figs. 3b and 4b show the corresponding HRTEM image. It clearly demonstrates that both the microplatelets and microspheres are actually assembled from primary ultrafine nanoplates. In Fig. 3c, the HRTEM image of the fringe of spherical particle exhibits good crystalline and clear lattice fringes, and visible lattice fringes of (110) planes with a lattice spacing of 0.275 nm were clearly observed. The HRTEM image of the microplate BiOCl particles is shown in Fig. 4c. Two sets of lattice fringes with a lattice spacing of 0.275 nm and 0.267 nm are clearly observed. The HRTEM image is viewed from (001) axis, which is corresponding to the (110) planes of the tetragonal system

of BiOCl. The corresponding SAED patterns of primary single BiOCl nanoplate and nanosphere were further examined and the results are shown in Figs. 3d and 4d, respectively. The unique pattern of diffraction spots can be indexed to the (110) and (200) plane, confirming its well-crystallized single crystal nature. The HRTEM observation further confirms that both platelet-like and spherical particles are BiOCl, which is well according to the aforementioned XRD result. On the basis of the above structural information, the percentage of highly reactive (001) facets in the BiOCl (0.06), BiOCl (0.18), BiOCl (0.22) and flower-like BiOCl are estimated to be 74, 85, 60 and 8.4 wt%, respectively. It is remarkable that the (001) facets in BiOCl (0.18) constitute more than 80 wt% of the total surface area.

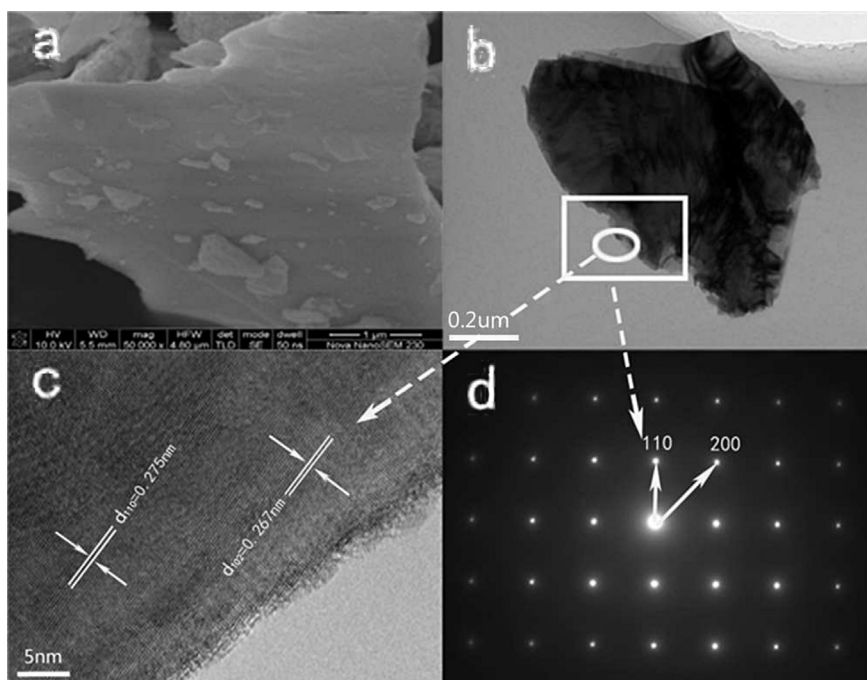


Fig. 4. High resolution (a) SEM and (b, c) TEM images of the platelet like particles, (d) shows the corresponding SAED pattern.

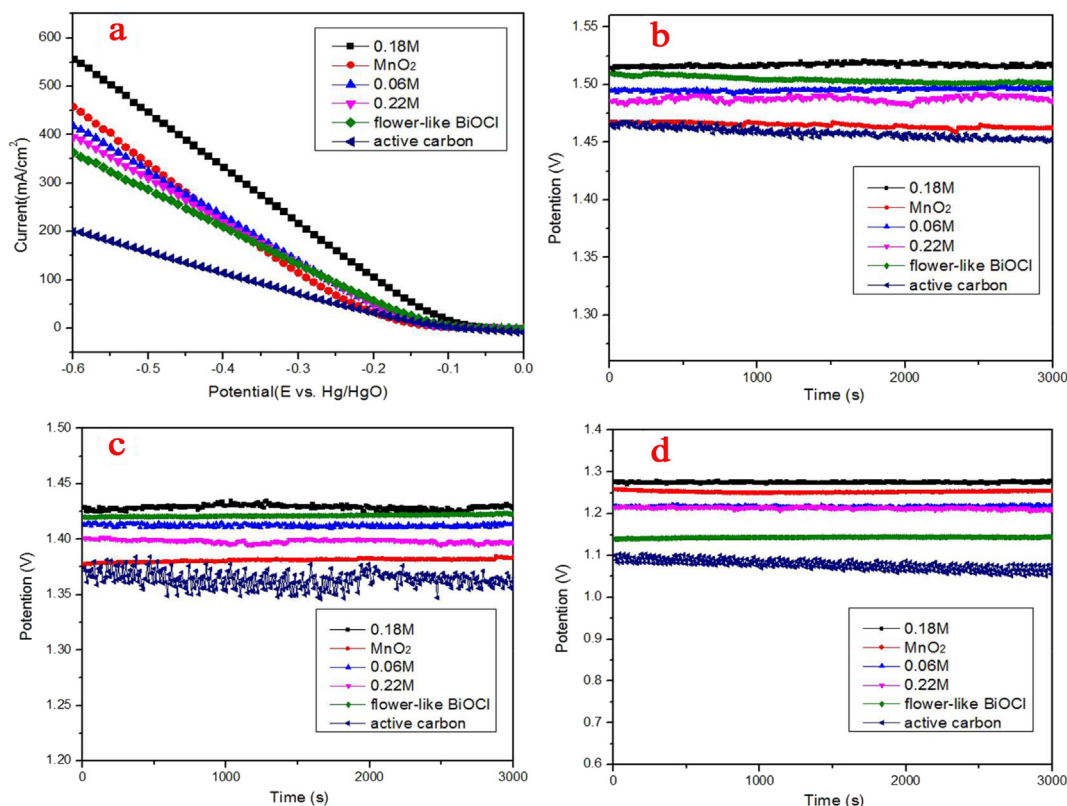


Fig. 5. (a) Polarization curve of the air electrode based on the different samples; discharge curve of the air electrode based on the catalyst with the current density of (b) 50 mA cm⁻², (c) 100 mA cm⁻², and (d) 200 mA cm⁻².

3.3. Electrochemical properties analysis

The cathodic polarization curve is shown in Fig. 5a. The decomposition potentials of the ORR (Oxygen Reduction Reaction, defined as the potential where the responsive voltammetric current approaches 1 mA) of all the samples are around -0.6 V vs. Hg/HgO. The polarization curves are different from sample to sample. The electrocatalytic activity of BiOCl (0.18) is relatively better than that of the traditional MnO₂. Noticeably the electrocatalytic activity of active carbon is inferior to those of BiOCl (0.18), MnO₂, BiOCl (0.06), BiOCl (0.22) and flower-like BiOCl (Table 1). This phenomenon shows that adding BiOCl catalyst can effectively improve the electro-chemical performance. Therefore, the BiOCl (0.18) sample performs slightly better than other samples as catalyst for air electrode application. Results from Figs. 1 and 5a indicate that the BiOCl (0.18) crystal is highly (001)-oriented. Therefore, we may conclude that BiOCl crystals having more (001) facets demonstrate better oxygen reduction catalytic activity. Fig. 5b–d display the discharge curves of the air electrode loaded with the BiOCl (0.06,

0.18, and 0.22), MnO₂, flower-like BiOCl, and active carbon samples at different current densities ($I = 50, 100$, and 200 mA cm^{-2}). We can see that the discharge voltage profile of the aluminum air battery differs a lot under different current density. As can be seen from Fig. 5b, when the discharge current density is 50 mA cm^{-2} , the stable potential of the air electrode with the BiOCl samples solid solution is over 1.47 V, which is a little higher than that of MnO₂ and active carbon samples. Obviously, with the increase of current density, the discharge voltage plateau decreases accordingly. Furthermore, the superiority of the electroactivity properties of as-prepared catalysts is more obvious under a higher current density of 100 mA cm^{-2} , as shown in Fig. 5c. The electrode potential after discharging for 3000 s is about 1.4 V, even higher than that using MnO₂ (1.37 V) and active carbon (1.35 V). However, when the discharge current density increases to 200 mA cm^{-2} , the stable potential of the air electrode with the BiOCl (0.18) sample is still higher than that of using MnO₂ solid solution (1.25 V). It's clear that under the same current density, the BiOCl (0.18) sample exhibits relatively the highest working potential window among all the samples. And this phenomenon becomes more obvious as the increase of current density. Therefore, the electrochemical performance of the BiOCl (0.18) sample is superior to other samples.

The redox behavior of the BiOCl (0.18) was investigated by cyclic voltammetry, and the results are presented in Fig. 6. The CV curve exhibits one pair of cathodic and anodic peaks under the potential window of -0.2–0.5 V. One well-defined oxidation peak was centered at approximate -0.05 V and one weak reduction peak was located at around 0.3 V in KOH solution. The CV patterns of the BiOCl (0.18) sample obtained under the potential window of -0.2–0.5 V exhibit electrical charge decay in the first cycle. This electrochemical polarization may be caused by slow charge transfer and ion diffusion, which is ascribed to the relatively large particle

Table 1
Performance comparison of air cathode electrodes at different potentials in 6 mol L⁻¹ KOH solution.

E (vs., Hg/HgO)/V	Current density (mA cm ⁻²)					
	BiOCl (0.06 M)	BiOCl (0.18 M)	BiOCl (0.22 M)	Flower-like BiOCl	MnO ₂	Active carbon
-0.1	2.36125	16.525	3.995	5.735	2.07975	3.465
-0.2	49.35	105.5	50.025	57	32.875	32.05
-0.3	138.35	217.65	133.225	132.4	114.6	71.125
-0.4	231.875	332.75	220	209.4	222.825	114.125
-0.5	323.25	447.25	310.5	287	339.75	157.85
-0.6	417.75	557	395	363	457.5	199

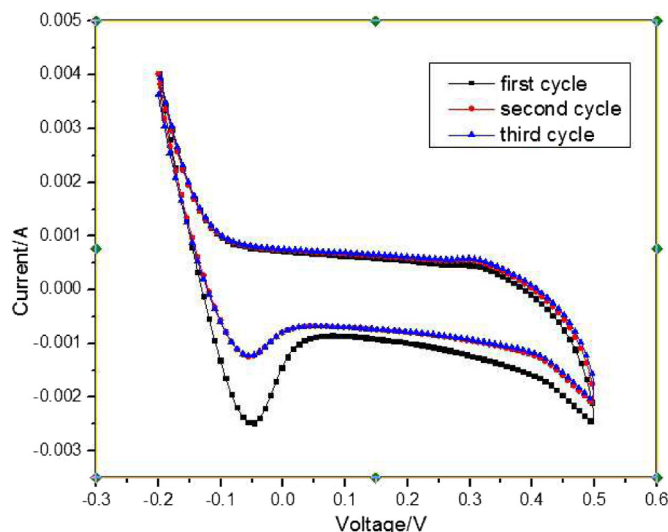


Fig. 6. Cyclic voltammograms obtained for BiOCl (0.18) electrocatalyst in 6.0 mol L⁻¹ KOH aqueous solution at 50 mV s⁻¹.

size of as-prepared BiOCl material as demonstrated in SEM image of Fig. 2. It is likely that the conversion reaction refines the particle size and leads to the formation of large fresh and active surface, an effect which has been observed for a number of conversion materials.

The effects of ORR rate on the polarization and discharging curves of the air-cathodes were quantitatively evaluated by the EIS analysis through establishing and fitting a reliable equivalent-circuit model. Typical EIS spectra, measured at the open-circuit

Table 2

The best-fitting values of equivalent-circuit elements in Fig. 7b for the impedance data shown in Fig. 7a.

E_{biased} (V)	E_{OCP}	-0.3
R_e (Ω cm ²)	2.213	2.212
Q_{int} ($\text{S cm}^{-2} \text{s}^{-n}$)	0.008527	0.05618
n ($0 < n < 1$)	0.7456	0.4131
R_{int} (Ω cm ²)	4.235	21.94
Q_m ($\text{S cm}^{-2} \text{s}^{-n}$)	0.002801	0.008408
n ($0 < n < 1$)	0.7438	0.8039
R_m (Ω cm ²)	0.3485	0.1661
W_o ($\text{S cm}^{-2} \text{s}^{-0.5}$)	0.8648	3.816×10^{-20}

potential (E_{OCP}) and -0.3 V on BiOCl (0.18), and the corresponding equivalent-circuit model are shown in Fig. 7. And the equivalent circuit for fitting EIS is also shown in Table 2. The analysis of Z_t for both air-cathodes in the potential region of interest is the sum of electrolyte, interfacial and charge-transfer impedances:

$$Z_t = Z_e + Z_{\text{int}} + Z_{\text{ct}} \quad (3)$$

$Z_e = R_e$ is the bulk solution resistance, Z_{int} is the interfacial impedance representing the overall ohmic effects and Z_{ct} is the charge-transfer impedance illustrating the overall kinetic effects. In Table 2, the bulk solution resistance, R_e , is very low and approximately independent of the biased potentials, which is a function of the distance between the Luggin capillary tip and the cathode. R_{int} , the interfacial resistances and cell components increases from 4.235 to 21.94 Ω with a higher over-potential. There are significant changes of the charge-transfer resistances R_m , thereby suggesting that potential has little impact on the charge-transfer resistance. Noticeably, the W_o changed obviously under high over-potential. We speculate that this effect significantly reduces the electrochemical charge-transfer resistance R_m and Warburg resistance W_o of BiOCl (0.18 M), leading to considerably enhancement of the ORR rate, which is consistent with the results from Fig. 5.

3.4. Electrocatalytic activity towards ORR

Fig. 8 shows the typical ORR current densities as a function of rotation rate ranging from 800 to 2500 rpm in 0.1 M KOH solution. The ORR operates under mixed kinetic-diffusion-controlled regime

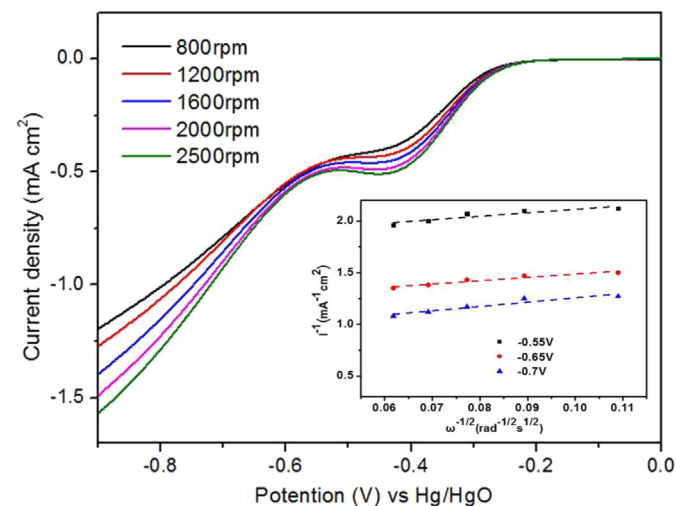


Fig. 8. ORR polarization curves of the BiOCl (0.18) obtained at different rpm (800 rpm–2500 rpm) in O₂-saturated 0.1 M KOH and a scan rate of 10 mV s⁻¹. Insets: Koutecky–Levich plots at different potentials (-0.55, -0.65, and -0.7 V).

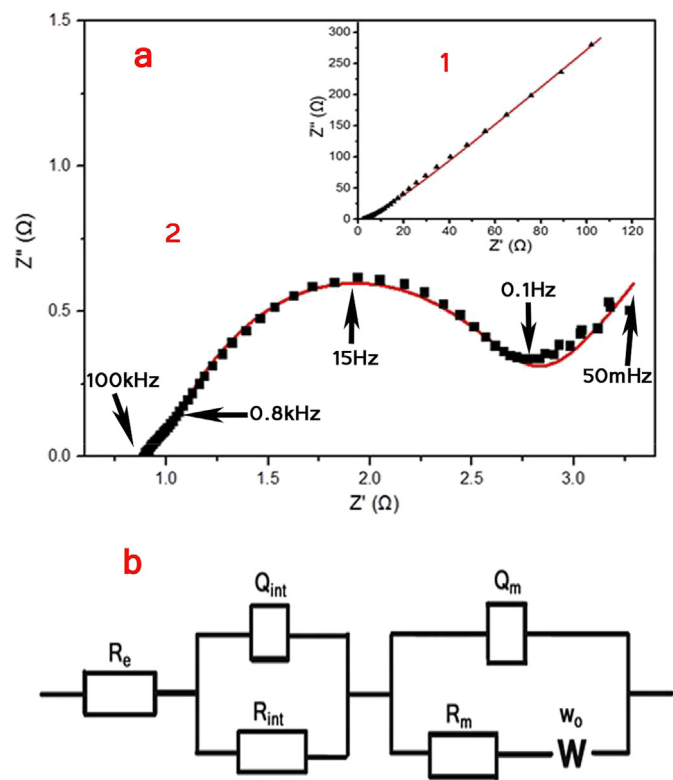


Fig. 7. Electrochemical impedance spectra measured at (a) (1) E_{OCP} and (2) -0.3 V for BiOCl (0.18 M) in 6 M KOH. (b) The equivalent-circuit model of BiOCl (0.18 M) for oxygen reduction.

Table 3

Kinetic parameters for catalytic reduction of oxygen at BiOCl (0.18)-modified glassy carbon (GC) electrodes in O₂-saturated 0.1 M KOH solution.

<i>E</i> (vs., Hg/HgO)/V	BiOCl (0.18)	
	K–L slopes	<i>n</i> (mol)
–0.55	3.36	2.67
–0.65	3.22	2.82
–0.7	4.0	2.30

in the potential ranges of –0.2 to –0.4 V and the potential lower than –0.6 V. In the potential range of –0.4 to –0.6 V, a current plateau was observed, indicating the domination of diffusion-limiting regime [36]. The Koutecky–Levich (K–L) plots were constructed for potentials ranging from –0.55 V to –0.7 V (inset of Fig. 8 and Table 3). These correlations are represented by the following equations:

$$i^{-1} = i_k^{-1} + i_l^{-1} \quad (4)$$

$$i_k = nFA\kappa C_{O_2} \quad (5)$$

$$i_l = 0.620n F A C_{O_2} D_{O_2}^{2/3} \nu^{-1/6} \omega^{1/2} \quad (6)$$

$$i^{-1} = 1/(nFA\kappa C_{O_2}) + 1/(0.620n F A C_{O_2} D_{O_2}^{2/3} \nu^{-1/6} \omega^{1/2}) \quad (7)$$

where *n* (mol^{–1}) is the electron transfer number per mole of reactive species, *F* (96,500 C mol^{–1}) is Faraday constant, *A* (cm²) is electrode area, *D*_{O₂} (cm² s^{–1}) is the diffusion coefficient of O₂ in 0.1 M KOH solution (=1.9 × 10^{–5} cm² s^{–1}), *ω* (s^{–1}) is rotation rate, *ν* (cm² s^{–1}) is kinetic viscosity of water (=0.01 cm² s^{–1}), and *C*_{O₂} (mol cm^{–3}) is the concentration of O₂ in 0.1 M KOH solution at 25 °C (=1.2 × 10^{–6} mol cm^{–3}). The constant 0.62 is applied when the

rotation speed is expressed in radius per second (rad s^{–1}). The number (*n*) of electrons transferred on the BiOCl (0.18) sample (Table 3) was calculated to be ~2.67, ~2.82 and ~2.3 respectively (~2.67 for potential –0.55 V, ~2.82 for –0.65 V, ~2.3 for –0.7 V), demonstrating a 2e[–] oxygen reduction process for the BiOCl (0.18) sample. This is also similar to the commercial carbon that is known to catalyze ORR in a 2e[–] process [37].

3.5. Catalytic mechanism

The BiOCl crystallizes in a tetrahedron structure as displayed in Fig. 9a, which can be derived from the fluorite (CaF₂) structure [38]. The unit cell is eight-coordinated, each Bi atom connecting to four O atoms and four Cl atoms in the form of an asymmetric decahedron constitutes. As shown in Fig. 9b and c, bismuth oxychloride has a layered structure consisting of [Bi₂O₂]²⁺ layers sandwiched between two slabs of chloride ions [39]. The [BiOCl] layers are stacked together by the van der Waals forces through the Cl atoms along the *c*-axis. As well known, the point defects are very important for catalysis. Point defect is cationic and anionic vacancies (oxygen vacancy). The catalytic properties are closely related to the vacancy concentration [40]. The types and quantities of defects in the semiconductors strongly affect their catalytic properties. As shown in Fig. 9d, oxygen species prefer to adsorb (α-oxygen) on the oxygen vacancy of the crystal plains, which is a kind of reactive oxygen species. BiOCl exposed with (001) facets have very good ability of oxygen storage and oxygen release for its abundant oxygen vacancies [38,41,42].

In the alkaline electrolyte, the electrochemical oxygen reduction reaction procedure can be mainly divided into two categories: one is a direct two-electron transfer process through the formation of HO₂ ions (or H₂O₂) as intermediate; another is a four-electron transfer process [43]. Generally, the ORR in alkaline media (with complete four-electron reduction) proceeds as follows:

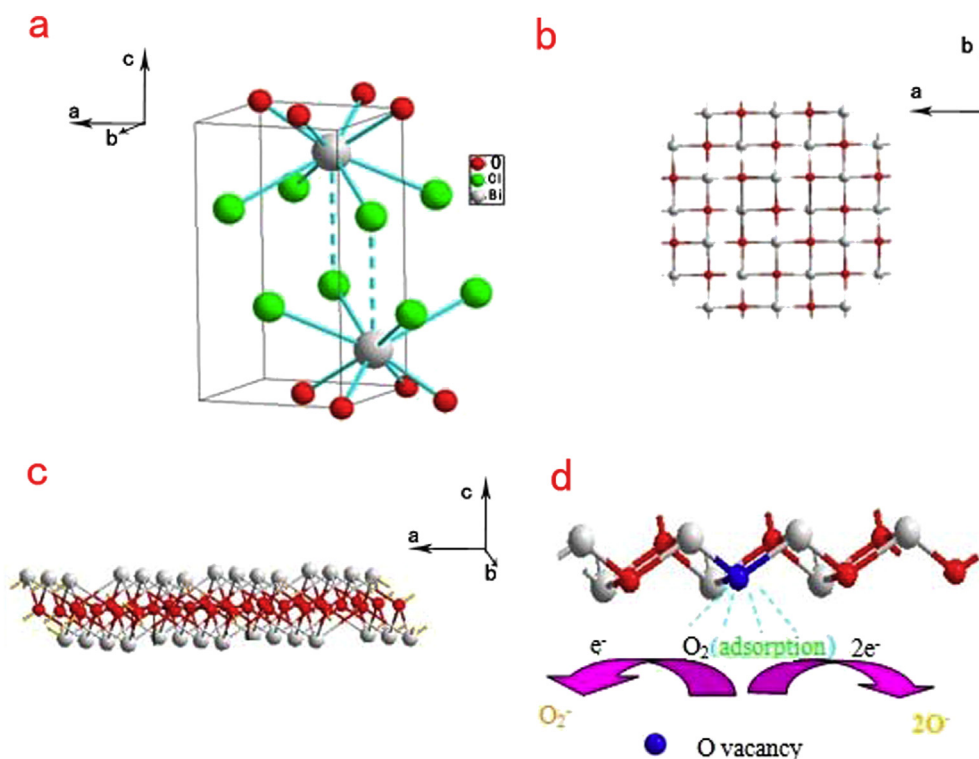


Fig. 9. (a) The unit cell of BiOCl; (b) [Bi₂O₂]²⁺ layers along with (001) direction; (c) [Bi₂O₂]²⁺ layers along with (010) direction; (d) oxygen vacancy adsorb oxygen to form reactive oxygen species.



While the two-electron procedure is as follows:



In both cases, the adsorption of molecular oxygen onto the active sites is the critical step during the reduction procedure. The ORR activation at a high discharge current density is considerably limited by the sluggish migration of molecular oxygen to active surface sites [44].

The real reaction mechanism of air electrode ORR is very complicated. In this work, according to Fig. 8 and Table 3, the oxygen reduction reaction of the current air electrode based on BiOCl adopts a 2-electron transfer process. So the formation of HO_2^- (or H_2O_2) (based on the reaction (9)) is the critical step during the electrocatalytic reaction. Generally speaking, the catalytic activity is largely determined by the capability of adsorbing oxygen species on the surfaces of the catalysts, which is in turn considerably affected by the oxygen vacancy of the crystals. That is, the intermediate HO_2^- species formed through the oxygen vacancies promote the decomposition of O_2 on the active sites of BiOCl. The higher the percentage of oxygen vacancy, the higher the catalytic activity of bismuth oxychloride would be. Therefore, high oxygen atom density in (001) facets is considered the fundamental cause of the increase of the oxygen vacancies in the crystal lattice [38]. So, the (001) facets of bismuth oxychloride was believed to be a major factor for HO_2^- species formation. Interestingly, the flower-like BiOCl has a high surface area of $35.91 \text{ m}^2 \text{ g}^{-1}$, which was much higher than that of the as-prepared BiOCl (0.06) ($2.8 \text{ m}^2 \text{ g}^{-1}$), BiOCl (0.18) ($2.7 \text{ m}^2 \text{ g}^{-1}$) and BiOCl (0.22) ($1.7 \text{ m}^2 \text{ g}^{-1}$) (Table 4). As well-known, the catalyst's particle size has profound effect on its catalytic properties. In addition to particle size, many factors may affect the catalytic performance, for example, the exposed crystal planes of the catalysts. In this study, the size of the BiOCl is very large, and the Brunauer–Emmett–Teller specific surface area (less than $3 \text{ m}^2 \text{ g}^{-1}$) is very small as compared with the nanosized flower-like BiOCl ($35.91 \text{ m}^2 \text{ g}^{-1}$). But the results as shown in Fig. 5 indicate that the catalytic activity of present BiOCl is much better than that of the flower-like BiOCl sample. It reveals that the key factors influencing the catalytic performance could be the highly reactive (001) facets. As deduced from the XRD and TEM results, the percentage of exposed (001) plane of the BiOCl (0.18) sample is approximately 80 wt%, a value much higher than that of the nanosized flower-like BiOCl sample ($\sim 8 \text{ wt}\%$). This might be the principle reason leading to the high electrocatalytic properties of the BiOCl catalysts prepared in the current experiment.

4. Conclusion

In summary, BiOCl micro-assemblies adopting a spherical and platelet-like morphology were successfully prepared by a facile hydrothermal method. The micro-assemblies were actually composed of ultrathin nanoplates. The as-synthesized BiOCl micro-assemblies were intensively examined as catalyst for air electrode of Al–air batteries. The results showed that the electro-catalytic properties are highly dependent on the precursor concentration. The BiOCl

(0.18) exhibited superior electro-catalytic property as compared with other samples. The oxygen reduction reaction of the BiOCl catalysts proceeds via a 2-electron transfer process. The electro-catalytic activity is closely related to the density of oxygen vacancy on the surface of the BiOCl samples.

Acknowledgments

This work was supported by the National Natural Science Foundation of China (21001117), and the Starting-Up Funds of South University of Science and Technology of China (SUSTC).

References

- [1] M.D. Paster, R.K. Ahluwalia, G. Berry, A. Elgowainy, S. Lasher, K. McKenney, M. Gardiner, *Int. J. Hydrogen Energy* 36 (2011) 14534–14551.
- [2] W.G. Colella, S.H. Schneider, D.M. Kammen, A. Jhunjhunwala, N. Teo, *J. Fuel, Cell Sci. Technol.* 8 (2011) 1–16.
- [3] Martin Winter, Ralph J. Brodd, *Can. J. Chem.* 104 (2004) 4245–4269.
- [4] F.Y. Cheng, Y. Su, J. Liang, Z.L. Tao, J. Chen, *Chem. Mater.* 22 (2010) 898–905.
- [5] T.H. Yang, S. Venkatesan, C.H. Lien, J.L. Chang, J.M. Zen, *Electrochim. Acta* 56 (2011) 6205–6210.
- [6] K.A. Friedrich, J. Kallo, J. Schirmer, G. Schmitthals, *Electrochem. Soc. Trans.* 25 (2009) 193–202.
- [7] G.R. Vallet, M. Saballus, G. Schmitthals, J. Schirmer, J. Kallo, K.A. Friedrich, *Energy Environ. Sci.* 3 (2010) 1458–1468.
- [8] S.H.H. Yang, H. Knickle, *J. Power Sources* 112 (2002) 162–173.
- [9] H. Wu, in: *World Non-Grid-Connected Wind Power and Energy Conference*, 2010, pp. 245–248.
- [10] Z.A. Zhuk, E.A. Sheindlin, V.B. Kleymenov, I.E. Shkolnikov, Y.M. Lopatin, *J. Power Sources* 157 (2006) 921–926.
- [11] G.M. Wu, C.C. Yang, *J. Membr. Sci.* 280 (2006) 802–808.
- [12] Y.G. Tang, H. Qiao, H.Y. Wang, P.P. Tao, *J. Mater. Chem. A* 1 (2013) 12512–12518.
- [13] Y.L. Cao, H.X. Yang, X.P. Ai, L.F. Xiao, *J. Electroanal. Chem.* 557 (2003) 127.
- [14] O. Oloni, S. Kumar, K. Scott, *J. Electron. Mater.* 41 (2012) 922–927.
- [15] M. Minakshi, K. Nallathambi, David R.G. Mitchell, *J. Alloys Compd.* 479 (2009) 87.
- [16] C.C. Yang, *Int. J. Hydrogen Energy* 29 (2004) 135–143.
- [17] R. Balgis, G.M. Anilkumar, S. Sago, T. Ogi, K. Okuyama, *J. Power Sources* 229 (2013) 58–64.
- [18] N. Ominde, N. Bartlett, X.Q. Yang, D.Y. Yang, *J. Power Sources* 195 (2010) 3984–3989.
- [19] I. Roche, E. Chaînet, M. Chatenet, J. Vondrák, *J. Phys. Chem. C* 111 (2007) 1434–1443.
- [20] F.H.B. Lima, M.L. Calegari, E.A. Ticianelli, *Electrochim. Acta* 52 (2007) 3732–3738.
- [21] F.H.B. Lima, M.L. Calegari, E.A. Ticianelli, *J. Electroanal. Chem.* 590 (2006) 152–160.
- [22] F.H.B. Lima, M.L. Calegari, E.A. Ticianelli, *Russ. J. Electrochem.* 42 (2006) 1283–1290.
- [23] Y.L. Cao, H.X. Yang, X.P. Ai, L.F. Xiao, *J. Electroanal. Chem.* 557 (2003) 127–134.
- [24] T.D. Chung, F.C. Anson, *J. Electroanal. Chem.* 508 (2001) 115–122.
- [25] T. Ohsaka, T. Watanabe, F. Kitamura, N. Oyama, K. Tokuda, *J. Chem. Soc. Chem. Commun.* 16 (1991) 1072–1073.
- [26] T. Okada, M. Yoshida, T. Hirose, K. Kasuga, T. Yu, M. Yuasa, I. Sekine, *Electrochim. Acta* 45 (2000) 4419–4429.
- [27] L. Mao, D. Zhang, T. Sotomura, K. Nakatsu, N. Koshiba, T. Ohsaka, *Electrochim. Acta* 48 (2003) 1015–1021.
- [28] F.C. Anson, C. Shi, B. Steiger, *Acc. Chem. Res.* 30 (1997) 437–444.
- [29] S. Ferguson-Miller, G.T. Babcock, *Chem. Rev.* 96 (1996) 2889–2908.
- [30] J.P. Collman, L. Fu, P.C. Herrmann, X. Zhang, *Science* 275 (1997) 949–951.
- [31] (a) S.X. Zhou, Y.X. Ke, J.M. Li, S.M. Lu, *Mater. Lett.* 57 (2003) 13–14; (b) J. Geng, W.H. Hou, Y.N. Lv, J.J. Zhu, H.Y. Chen, *Inorg. Chem.* 44 (2005) 8503–8509.
- [32] S.J. Wu, C. Wang, Y.F. Cui, T.M. Wang, B.B. Huang, X.Y. Zhang, X.Y. Qin, P. Brault, *Mater. Lett.* 64 (2010) 115–118.
- [33] K. Li, Y.L. Xu, Y. He, C. Yang, Y.L. Wang, J.P. Jia, *Environ. Sci. Technol.* 47 (2013) 3490–3497.
- [34] (a) C.R. Michel, N.L. López-Contreras, A. Cruz-Hernández, A. Yocupicio, C.D. Rivera-Tello, *Electrochim. Soc.* 33 (2010) 149–151; (b) H. Peng, C.K. Chan, S. Meister, X.F. Zhang, Y. Cui, *Chem. Mater.* 21 (2009) 247–252.
- [35] F. Chen, H. Liu, S. Bagwasi, X. Shen, J. Zhang, *J. Photochem. Photobiol. A: Chem.* 1 (2010) 76–80.
- [36] J. Sunarso, A.A.J. Torriero, W. Zhou, P.C. Howlett, M. Forsyth, *J. Phys. Chem. C* 116 (2012) 5827–5834.
- [37] R.B. Valim, M.C. Santos, M.R.V. Lanza, S.A.S. Machado, F.H.B. Lima, M.L. Calegari, *Electrochim. Acta* 85 (2012) 423–431.

Table 4
The Brunauer–Emmett–Teller surface areas of the prepared BiOCl catalysts.

	BiOCl (0.06)	BiOCl (0.18)	BiOCl (0.22)	γ -MnO ₂	Flower-like BiOCl
$\text{m}^2 \text{ g}^{-1}$	2.8	2.7	1.7	28	36.0

- [38] L.Q. Ye, L. Zan, L.H. Tian, T.Y. Peng, J.J. Zhang, Chem. Commun. 47 (2011) 6951–6953.
- [39] (a) K.G. Keramidas, G.P. Voutsas, P.I. Rentzeperis, Z. Krist., Cryst. Mater. 205 (1993) 35–40;
(b) M. Guan, C. Xiao, J. Zhang, S. Fan, R. An, Q. Cheng, J. Xie, M. Zhou, B. Ye, Y. Xie, J. Am. Chem. Soc. 135 (2013) 10411–10417.
- [40] J.M. Ma, X.D. Liu, J.B. Lian, X.C. Duan, W.J. Zheng, Cryst. Growth Des. 10 (2010) 2522.
- [41] (a) Y.Q. Lei, G.H. Wang, S.Y. Song, W.Q. Fan, H.J. Zhang, Cryst. Eng. Commun. 11 (2009) 1857–1862;
(b) L. Li, N. Sun, Y. Huang, Y. Qin, N. Zhao, J. Gao, M. Li, H. Zhou, L. Qi, Adv. Funct. Mater. 18 (2008) 1194–1201.
- [42] (a) F. Yan, T.J. Zhu, M.O. Lai, L. Lu, Scr. Metal. 63 (2010) 780–783;
(b) Y. Zheng, F. Duan, M. Chen, Y. Xie, J. Mol. Catal. A: Chem. 317 (2010) 34–40.
- [43] C.C. Yang, S.T. Hsu, W.C. Chien, M. Chang Shih, S.J. Chiu, K.T. Lee, C.L. Wang, Int. J. Hydrogen Energy 31 (2006) 2076–2087.
- [44] M.A. Kostowskyj, D.W. Kirk, S.J. Thorpe, Int. J. Hydrogen Energy 35 (2010) 5666–5672.